

Debadutta Subudhi¹, Prasanna K Routray¹, and Manivannan Muniyandi¹

¹Affiliation not available

April 16, 2024

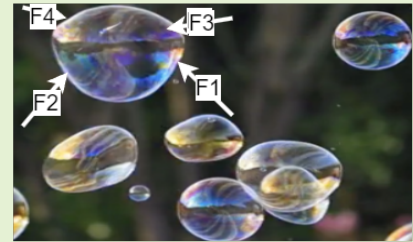
Subblescope: A Thin Film Haptic Sensor

Debadutta Subudhi, Prasanna K. Routray and Manivannan Muniyandi

Abstract—Vision-based haptic sensors have become an increasingly common tool for providing both coarse and delicate tactile feedback in robotic fingers. We present a soft, affordable, vision-based tactile sensor named Subblescope, which provides the magnitude and direction of the applied force. The sensor consists of a single layer of Ecoflex incorporating an air bubble inside it, which is injected into the sample while curating to stabilize the bubble. An LED array lights the elastomer, while a camera records the shape change of the bubble during normal and shear force interaction. The sensor is calibrated using a micro-tensile UTM. In the case of normal loading, the sensor has a sensitivity of $248.6 \mu\text{N}$ over a range of 0.02 N to 2.9 N , with a repeatability of 1.09% at 0.6 N , and hysteresis of $26.23 \mu\text{J}$ between 0.1 N to 0.6 N . In the case of shear loading, the range is 0.02 N to 0.15 N with a sensitivity of $31.31 \mu\text{N}$, better than the existing vision-based haptic sensors.

The multidirectional loading onto the sensor provides 3D shapes of the bubble simulated in COMSOL. The present concept and design are more compliant for sensing bi-directional force interactions while maneuvering interactive surfaces. Multiple bubbles can be populated in the elastomer for further study towards spatio-temporal sensing.

Index Terms—Bubble, Hyperelasticity, Camera Based Sensor, Vision Based Haptic Sensor, Optomechanics, Micro UTM.



I. INTRODUCTION

VISION based haptic sensors offer the potential for sensitive finger touch, enabling accurate manipulation. Contact-force interaction is involved in the manipulation of objects by either a human finger or a robotic finger. The magnitude of the contact force is influenced by factors such as the physical properties of the contact surface (e.g., softness or hardness) and the qualities of the materials involved, including texture, friction, and shape. Furthermore, the interaction might be either passive or active. In passive contact, the interface does not react to the applied force, but in active engagement, the interface reacts to the applied force. The human hand is mostly engaged in both passive and active interactions because of the existence of mechanoreceptors [1]. Similarly, a robotic finger requires a human finger-like touch capability.

The studies in literature demonstrate the advancement of haptic sensors [2] designed to measure contact forces. The measurement of the contact force uses resistive and strain gauge elements [3], [4], [5], [6], [7], capacitive sensing [8], [9], [10], [11], [7], the principle of magnetic sensing [12], ferroelectric [13], triboelectric [14], and opto-resistive [15], [16] sensors. Recently, vision-based haptic sensors [17], [18], [19], [20], [21], [22], [23], [24] have evinced various solutions towards tactile sensing. The vision-based haptic sensor (VHS) is a class of optical sensors widely applied to robotic perception for environmental probing towards kinaesthetic and tactile inputs. The kinesthetic perception is based on the reaction forces from the environment and tactile perception is based

on the texture [25] of the surface. The basic building blocks of the VHS are shown in Fig.1.

The VHS employs optical touch sensing or visuotactile sensing (VTS) components, which have been advancing since 1950 to determine shape, texture, force, and temperature. The VTS consists of five essential components: a light source, an optical guide, a mirror layer, a reflective layer, and an elastomer serving as the contact body (CB). The mechanics of the CB and its constituents are the most important factors in deciding the tactile measurements. The VTS in pedograph [26] records the pressure map of the feet with a CB of polyvinylchloride (PVC) proving a pressure 0 MPa to 0.3 MPa . A similar design [27] has silicon rubber as CB, acrylic array as light ray guider (LRG), and phototransistor array to record the contact pressure. The CB is in use for remote manipulators towards grasping and slip detection using translucent polyurethane rubber [28], clear elastomer [29] where optic fiber bundle was employed to transmit the data to the processing unit. Later in the 1990s, a finger-shaped VTS design was put in to detect contact location using an elastic cover separated by air from the optical waveguide [30]. The first marker layer (ML) based finger-shaped VTS was designed by embedding a grid of dots on the CB [31] to estimate object geometry. A feeler array consisting of soft rubber cones, firm rubber columns as CB, and pyramidal projected acrylic board has been used to construct the early stage force and moment measurement utilizing VTS [32]. The 3D force application is mapped with contact area as I/O function. These VTSs work on the principle of total internal reflection from CB deformation due to contact and external force. One key observation in preliminary VTSs is that the internal structure CB is not modified.

D. Subudhi, P. K. Routray, and Manivannan M. are with the Touch Lab, Center for Virtual Reality and Haptics, Indian Institute of Technology Madras, India, 600036 (e-mail: prasanna.routray97@gmail.com, dev.subudhi49@gmail.com, mani@iitm.ac.in)

The new form of VTSs subsumes internal changes to the CB to measure force and torque vector field. A typical case is to infuse visible markers into the CB for capturing vector fields using cameras. GelForce [33] was built by infusing red and blue spherical bead layers separated by 1.5 mm to capture the force field. GelForce was further modified as VHS for dexterous manipulations with a spatial resolution of 5 mm and a force resolution of 0.3 N in 3D [34]. The input-output mapping for GelForce is defined as follows:

$$F = f(U), F = (H^T H)^{-1} H^T, \quad (1)$$

where F is the force vector, H is the conversion matrix obtained during calibration to applied forces along and cross Cartesian directions, U is the movement vector obtained from the bead motion obtained from the camera module (CM).

The VHS is enabled for temperature sensing by adding a thermo-sensitive paint layer whose color changes according to change in temperature from 31.5 °C to 34.5 °C depending on the paint property [35]. The function mapping for VHS in this case is defined as: $T = g(h)$. Where T is the object temperature, h is the hue in the image captured by CM.

Our study focuses on the introduction of fluid into the CB and its possible usage for measuring force and roughness. Additional experimentation is required to investigate the measurement of both shape and temperature.

The bubble has several applications in the fields of mechanics, medical imaging, and soft robotics. The phenomenon of a bubble rupturing in the elastomer is examined to analyze anomalies (fractures) in the elastomer [36]. Furthermore, the maximum pressure occurring inside an expanding bubble within an elastomer was used to determine the elasticity and surface tension of the elastomer [37], [38]. The motion of bubbles inside a portable microfluidic device facilitates micromixing in fluid systems [39]. The presence of microbubbles in the bloodstream enhances the ability to visualize the cardiac chambers during ultrasound imaging of the heart in the field of medical imaging [40]. Nonetheless, in the field of soft robotics, the manipulation of air pressure inside a soft robotic frame allows for delicate grasping [41], crawling [42], and swimming [43]. In each of the aforementioned scenarios, the fluid continues to be in a state of motion. The novelty of the current study lies in the confinement and stabilization of the fluid (air) inside the elastomer for the purpose of force sensing.

The paper is structured in the following manner. Section-II describes the related works of vision-based tactile sensors, focusing on the measurement metric followed by the problem statement. The proposed sensor configuration is in the section-III. Section-IV outlines the design and fabrication of the sensor. Section-V explains the methodology for simulation setup, algorithm involved, and sensor calibration setup. Section-VI covers the results from simulation and sensor calibration. Section-VII discusses various aspects of the sensor including challenges, applications, and tactile modalities followed by the conclusion in section-VIII.

II. RELATED WORKS

The development of gelForce lead to a series of modification to internal structure of CB to measure force and torque

information through the standard calibration procedure and machine learning approaches. TacTip uses papillae in CB for sensing force [44], [21] with a spatial resolution of 0.2 mm with sensing range of 0.1225 N to 11.27 N for normal, and 0.1225 N to 1 N for shear loading (F_S). The gelSight [17], and its miniaturized version called gelSlim [18] use printed black dots inside CB to record the deformation with a spatial resolution of 1.1 mm, a resolution less than 0.05 N. However, the practical range and resolution of detected force in normal and shear are not discussed. The gelSight and gelSlim are best known for object shape recognition with finer details. Similarly, the spatial resolution of OmniTact and gelTip are 0.4 mm, and 10 mm respectively, whereas the typical force sensor metrics are not mentioned explicitly. Similar to omniTact, InSight [23], and MinSight [24] incorporate a single layer of CB made up of Ecoflex 00-30, Aluminum powder (65 μ m) and flake(65 μ m)) that is placed over the thumb-shaped skeleton (AlSi10Mg-0403 aluminium alloy) to increase the robustness. The InSight, and MinSight use machine learning approach using an automated test bench showing spatial resolution of 0.4 mm, and 0.6 mm respectively. The force range is reported to be 0.03 N to 2 N, 0.06 N to 2 N respectively for normal loading (F_N). The introduction of aluminum inside the Ecoflex reduces the compliance (deformability) of the CB.

Problem Formulation: The literature on VHS explores the quantification of various tactile and haptic stimuli, including shape, proprioception, force, torque, and temperature. Nevertheless, it exhibits inadequate sensitivity and lacks comprehensive sensor characterization. Furthermore, the VHSs undergo passive loading in only one direction, and there has been no investigation into the performance of these sensors under bi-directional loading. Bi-directionality refers to the ability to monitor both applied and reactive forces exerted on a surface (e.g. organ palpation). Hence, it is imperative to create affordable and sustainable sensors that can accurately replicate the fine tactile abilities of human fingers on robots and prosthetic fingertips. Some of the studies in the literature demonstrate the alteration of CB through fillers and markers. Nevertheless, the addition of fillers reduces the ease of deformability of CB, resulting in decreased sensitivity. Whereas markers do not affect deformability, but neither enhance it. The current work reports enhancing the sensitivity of CB by infusing it with a singular bubble, allowing for the measurement of 3D forces for delicate touch applications and bi-directional sensing.

This study introduces a single bubble that has been stabilized within a single layer of EcoFlex 00-31. In addition to functioning as an optical marker within the CB, it enhances the CB's compliance, thereby enabling bidirectional sensing for a variety of tactile stimuli. Using COMSOL 6.1, the study analyzes the multiaxial loading on the bubble-infused elastomer. Hyperelastic models of the sensing material are developed utilizing micro-UTM. Calibration is performed on the sensor in order to determine the static and dynamic characteristics of normal and shear forces. The developed sensor is referred to as 'Subblescope', from the fact that the tactile inputs to the sensor are seen from deformation of single bubble which is the novelty.

III. PROPOSED SENSING PRINCIPLE

The robotic fingertips lack fine touch and active sensing capability similar to human fingertips involving forces less than 1 N [45]. The presence of bubbles with specific internal pressure inside a flexible elastomer causes the elastomer to weaken and allows it to deform under such lower forces compared to an elastomer without any bubbles as shown in Fig.2a. However, the bigger challenge is to stabilize and control the size of a bubble inside an elastomer, which is discussed in section-V. The basic sensing principle is the variation of bubble shape to external forces, tracked by a camera.

A. Sensor Configuration

The Subblescope constitutes a number layers with various functions. These layers include a thin composite rubber layer as protective layer (PL), Ecoflex 00-31 as CB, bubble as ML, conical acrylic body as LRG with a cylindrical acrylic substrate (28 mm×2 mm) on top of the LRG to hold the CB, pi-camera module, and programmable LED ring with eight LEDs as illumination layer (IL), shown on right side of Fig.1. The hierarchical structure of VHS is shown on the left side of Fig.1.

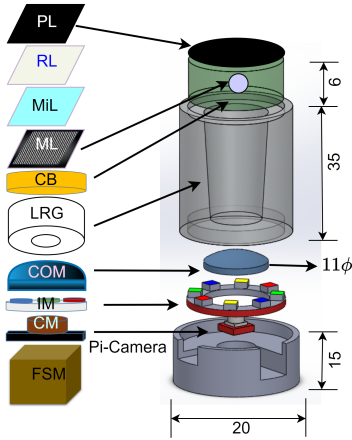


Fig. 1: Hierarchical structure of Vision-based Haptic Sensor (VHS): Protective Layer (PL), Reflective Layer (RL), Mirror Layer (MiL), Marker Layer (ML) Contact Body (CB), Light Ray Guider (LRG), Collimator (COM), Illumination Module (IM), Camera Module (CM), and Force Sensing Module (FSM). The Subblescope does not include the RL, MiL, and FSM. The dimensions of each part are in mm.

The infusion, stabilization, and optimal size of bubble inside an elastomer plays a crucial role during the design and fabrication of Subblescope described in III-B.

B. Bubble Stabilisation

The bubble stability inside the elastomer depends on the viscosity (μ_e) and surface tension (σ_e) of the elastomer while injecting the air bubble. The dimensionless parameters Eötvös number (Eo), and Morton number (Mo) are used to obtain μ_e and σ_e [46] using equation 2 as follows:

$$E_o = \frac{F_b}{F_s} = \frac{g(\rho_e - \rho_b)L_c^2}{\sigma_e} \quad (2)$$

$$M_o = \frac{F_v}{F_s} = \frac{g\mu_e^4(\rho_e - \rho_b)}{\rho_e^2\sigma_e^3}$$

where, F_b is the buoyancy force, F_v is the viscous force, F_s is the force due to surface tension. The density $\rho_e = 1070 \text{ kg m}^{-3}$ for EcoFlex 00-31 is taken from the datasheet. σ_e is the surface tension of the elastomer before curing, $\rho_b = 1.29 \text{ kg m}^{-3}$ is the density of the air bubble at NTP, and $g = 9.8 \text{ m s}^{-2}$ is the acceleration due to gravity. The diameter (d_b) of the bubble is based on the injected air volume (V_{inj}) given by $d_b = [\frac{6V_{inj}}{\pi}]^{1/3}$. A 0.5 mL insulin syringe of 31G grade with 40 units capacity is used to inject the air bubble inside the elastomer. The diameter of the 31G grade needle (d_n) is 0.133 mm. The injected air volume for bubble formation is 5 units (0.0625 ml) which corresponds to a bubble diameter (d_b) of 5 mm. Moreover, the diameter of the bubble by the needle injected into the elastomer is given by[46]:

$$d_b = \frac{6\sigma_e d_n}{\rho_e g} \quad (3)$$

Now, for a bubble diameter of 5 mm the surface tension of the elastomer using (3) is 1.644 Nm . The threshold value of the viscosity with the surface tension of 1.644 Nm is obtained using $M_o = 1$, resulting in a viscosity of 4693.38 cPs . Therefore, the bubble has to be injected into the elastomer during curing at a viscosity of $\mu_e \geq 4693.38 \text{ cPs}$ and less than one-third of the curing time, which is four hours for Ecoflex 00-31. Therefore, a viscosity of 4800 cPs is essential to stabilize the bubble within the elastomer. Moreover, the Eötvös number for $\sigma_e = 1.644$ is 0.0044 , signifying the dominance of surface tension over the buoyancy force of the bubble. This ensures the stability of the bubble inside the elastomer. Therefore, the viscosity curve of elastomer with time is essential in determining the time at which the bubble should be injected (t_{inj}) into the elastomer during curing. The viscosity of the EcoFlex 00-31 is determined by the vibroviscometer (SV-10, range 0.3 cPs to 10 000 cPs) with a sample volume of 35 mL. The viscosity varies quadratically with time as given below.

$$F = 1.656 \times 10^{-4}t^2 + 7.554 \times 10^{-1}t + 1.962 \times 10^3 \quad (4)$$

During the process of curing, the elastomer starts solidifying around 2800s. Thereafter, the viscosity cannot be measured. After 2800s the sample starts solidifying, hence the viscosity can not be measured thereafter. The quadratic relation allows us to get the time at which the sample attains a viscosity of 4800 cPs which is found to be 2445.54 s or time from bubble injection ($t_{inj} = 40.76 \text{ min} \approx 41.0 \text{ min}$). The pressure difference between elastomer and bubble can be found as ($4\sigma_e/r_b = 4 \times 1.644/(0.005/2) = 2630.4 \text{ Pa}$). The factor of '4' accounts for the existence of inner and outer film surfaces. The process control parameters V_{inj} and t_{inj} are crucial in the fabrication of bubble infused VHS.

IV. SENSOR FABRICATION

The elastomer is prepared by thoroughly mixing the EcoFlex 00-31 solutions A and B for 2 minutes. The mixed solution is subjected to degassing inside a vacuum chamber with a pressure of 700 mmHg till the sample is free from the dissolved process gases generated during mixing. The degassed solution is poured into the acrylic cylindrical mold

cavity, made by a conventional CNC milling machine. The sample dimension (diameter \times height) is 28.5×6 mm. The curing time of the sample is four hours, however, the transition happens after one hour, when the sample begins solidifying as observed from the viscometer. Hence, the injection of air into the elastomer is carried out after 30 min, using a 31G syringe at the center part of the elastomer. The solidification is faster at the boundary and it spreads to the center gradually, which helps the bubble to be contained in the elastomer supported by the surface tension and viscosity of the elastomer on the surface of the bubble. After the bubble injection, the sample is allowed to cure at normal temperature and pressure (NTP) as shown in Fig.2c.

The pi-camera (1080p-HD) captures bubble contour in the presence of a diffused light that passes through the acrylic diffuser. The boundary of the bubble is illuminated by pink light using the programmable LED ring (8-bit WS2812-5050 RGB). However, any combination of light can be used to observe the deformation gradient at the boundary of the bubble. The light rays pass through an acrylic diffuser to have a diffused refraction of light inside the elastomer. The shape change in the bubble is captured by a Raspberry Pi camera followed by a collimator, placed above the camera as shown in Fig.1. The PL is prepared from a thin black pigmented soft rubber and the light diffuser is painted with black color from outer and inner boundary to stop external light interference on the sensor. The polylactic acid (PLA) casing protects the sensor while exposing a circular sensing area of 315 mm^2 near the injected bubble.

A. Mechanical Characterization

The mechanical characterization is to determine the hyperelastic behavior of the elastomer in the presence and absence of bubbles. Three standard ASTM-IV cylindrical ($28.5 \text{ mm} \times 12 \text{ mm}$) EcoFlex 00-31 specimens are tested under compression load using a micro-UTM having a range of force from 20 mN to 2 kN. Four hyperelastic models: Mooney Rivlin, Neo-Hookean, Yeoh, and Ogden [47] are fitted to the experimental data using parameter optimization module in COMSOL 6.1. as shown in Fig.2a. The Yeoh and Ogden are best-fit material models with lower root mean square error (RMSE) as evident from Fig.2b. Consequently, we have considered the Yeoh model for the simulation studies with material constants $C1 = 0.12505 \text{ MPa}$, $C2 = 0.06929 \text{ MPa}$, $C3 = 36.488 \text{ MPa}$.

B. Optical Characterisation

The optical characterization of the EcoFlex 00-31 is for finding the optical path from the light source to the bubble for clear visibility of the bubble's boundary. Therefore the refractive index of the elastomer plays a crucial role along with the refractive index of the acrylic body through which the light rays travel. Four samples of dimension ($10 \text{ mm} \times 10 \text{ mm} \times 2 \text{ mm}$) are placed under Abbe-refractometer as shown in Fig.2d. Monobromo-naphthalene ($\mu = 1.66$) is used as a standard solution for obtaining the

average refractive index ($\mu_e = 1.44$) of the elastomer.

Optical Path: The refractive index (μ_a) of acrylic body is 1.49. Therefore, a negligible refraction happens for the light rays passing from the acrylic body to the elastomer. The inner and outer boundaries of LRG are painted in black color. The light rays pass from the edge of LRG to the elastomer through the air medium, bending the light rays by 44° by Snell's law, thereby illuminating the boundary of the bubble as shown in Fig.2e. The light rays refracted from the outer layer of the bubble are absorbed by the black rubber layer, placed on the top of the elastomer as a PL. The boundary expands with external load, altering the refraction phenomenon captured by the CM. The collimator has a diameter of 11 mm and a focal length of 21 mm. The distance of the center of the bubble from the collimator is 43.5 mm.

Wavelength of the light: The LED is programmed to illuminate a pink color, containing 100% red, 75.3% green, and 79.6% blue. This combination creates a clear bubble boundary besides other combinations of RGB triplets. The thickness of the thin film boundary between air and the elastomer in the reference configuration or initial configuration is 0.2 mm, as obtained from the image captured by the camera in Fig.2e.

V. METHODOLOGY

A. Simulation setup

The simulation aims to determine morphological shapes of the bubble resulting from multiaxial loading. The multiaxial loading consists of applying a normal, radial, and shear force to the elastomer, which is positioned on an acrylic substrate with a spherical air domain. Hence, the structural configuration (dimensions are in mm) consists of a cylindrical Ecoflex elastomer with a single bubble on a stationary glass substrate, as seen in Figure 2g. The boundary conditions consist of Gaussian loads applied to the elastomer in both the normal and radial directions, as seen in Figure 2h. A shear stress of 0.5 N is applied to the top of the elastomer. The elastic constants for elastomer are the Yeoh parameters, explained in section-IV-A. The air contained inside the elastomer is under hydrostatic condition, and exhibits the characteristics of an elastic material [48] with a modulus equal to the internal pressure 2.6340 kPa, and poisson ratio $\nu = 0.49$. The structure is homogenous as both air and elastomer are homogenous. The finite element analysis (FEA) is performed using COMSOL 6.1 to determine the deformation of the bubble to the boundary load. The simulation facilitates the resolution of experimental intricacies that need the use of various camera viewpoints.

B. Algorithm

The algorithm computes area of bubble's contour along with its perimeter, centroid, and length of semi-major (a), and semi-minor (b) axes. The raw image is converted to a grayscale image followed by the contrast-limited adaptive histogram equalization (CLAHE) with a clip limit of five to enhance the contrast of the region of interest (ROI) including the boundaries of the bubble. The ROI is obtained by putting the

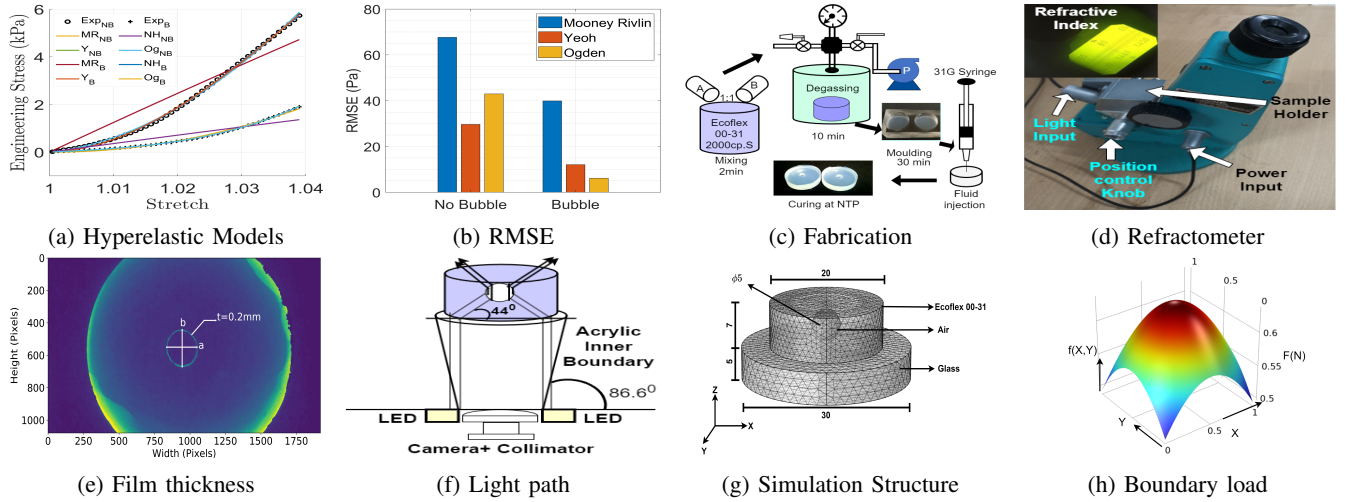


Fig. 2: **a.** MR-Mooney Rivlin, NH-Neo-Hookean, Y-Yeoh and Og-Ogden models are fitted to the stress-stretch curve for bubble (B) and non-bubble samples (NB). **b.** Mean square error (MSE) of the fitted curve from the experimental data for MR, Y, and Og models. **c.** The fabrication of Subblescope. **d.** The measurement of the refractive index of Ecoflex 00-31 sample ($10 \times 10 \times 2 \text{ mm}^3$) using the Abbe-refractometer. **e.** The film thickness has an average value of 0.2 mm in the initial configuration of Subblescope. **f.** The light path from the LED to the bubble. **g.** The simulation setup constitutes glass, air, and elastomer. The dimensions are in mm. **h.** The multiaxial loading is applied as the Gaussian distribution boundary load in both normal and radial directions to the elastomer, and 0.5 N of shear load on the top surface of the elastomer.

bounding box around the bubble. The threshold operation with a minimum and maximum value of 90 and 255 respectively is applied to segregate the bubble boundaries (inner and outer) from the background. The minor gaps if present are filled through closing operation. After which, the Gaussian blurring of the image results in a smooth bubble boundary. The Sobel gradient [49] applied to the blurred image creates well-defined inner and outer boundaries of the bubble. The final contour detection is applied to the gradient image containing the magnitude of the gradient using computer vision libraries in Python. Fig.3 shows the initial and processed images for a particular frame from the captured video.

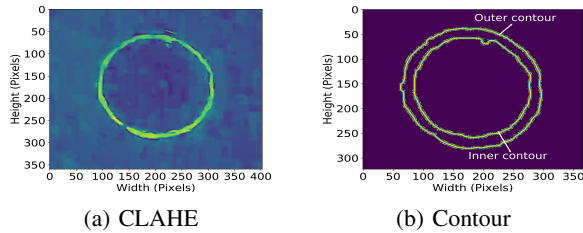


Fig. 3: **a.** The CLAHE on a typical video-frame that enhances the pixel contrast at the boundaries. **d.** The contour of the bubble with the outer and inner boundaries.

C. Characterization

The calibration of the Subblescope for normal and shear loading is carried out on a micro-UTM. The precise and controlled displacement of the indenter applies forces on the Subblescope in the normal direction as shown in Fig.4a. The shear force calibration is achieved by a fixture arrangement of magnetic base, X- θ rotary table, and rectangular-slotted cuff to hold the Subblescope along X-direction, whereas the indenter moves in Z-direction as shown in Fig.4b.

The calibration provides the static and dynamic characteristics of the sensor. The static characteristics for normal

force application include resolution, range, sensitivity, offset, repeatability, accuracy, linearity, and hysteresis. Whereas for shear force, resolution, range, sensitivity, and offset are evaluated. The characteristics such as repeatability, accuracy, and hysteresis do not change for an isotropic material irrespective of loading conditions. The dynamic characteristics are determined by analyzing the step response of Subblescope.

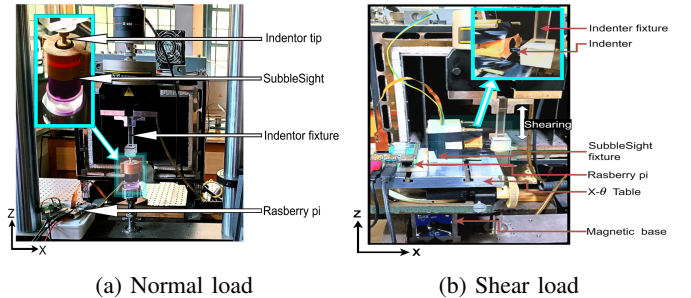


Fig. 4: **a.** The calibration setup for normal compressive load application by the fixture holding a mushroom-shaped indenter onto the Subblescope. **b.** The calibration setup for applying shear to the Subblescope

VI. RESULTS

The results encompass both the static and dynamic characteristics of Subblescope, as well as simulation.

A. Simulation Results

The Subblescope is designed to sense normal and shear forces but not the radial force due to manufacturing constraints. Furthermore, the actual forces are multiaxial in nature. Hence, our simulation study demonstrates the morphological changes of the bubble under multiaxial loading conditions. Under F_N , width of minor axis of the bubble decreases while the width of major axis increases, and vice versa during application of the radial load (F_R). F_S causes

the bubble to move along a line of action. The impact of different loading circumstances on the deformation of the bubble's shape is seen in Figure 5.

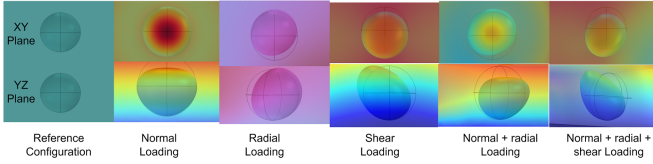


Fig. 5: The simulation results for the bubble deformation under various loading conditions: individual F_N , F_R , F_S , the combined normal with radial load ($F_N + F_R$), and combined normal, radial, and shear load ($F_N + F_R + F_S$)

B. Characterization Results

Normal loading:

An increase in displacement of the indenter in a direction perpendicular to the surface results in a corresponding uniform increase in the shape of the bubble, as seen in Figure 6a. The calibration curve is obtained by functionally mapping the force gauge reading from the micro-UTM and the area of maximum contour, as seen in Figure 6b. The indenter advances in steps of 0.1 mm until it achieves a displacement of 2.3 mm, which corresponds to a force gauge measurement of 4.5 N. However, the bubble's border becomes indistinguishable beyond a force of 3 N, as a result of a decrease in thickness of the film. The calibration curve is represented by a quadratic equation as seen in equation (5).

$$F = 1.364 \times 10^{-9} Cb_m^2 - 0.000108Cb_m + 2.02 \quad (5)$$

where, $F[N]$ is force gauge reading, $Cb_m(\text{Pixel}^2)$ is maximum area of contour of the bubble.

The sensor is validated by eight random load cycles. The Subblescope's response to a single random load cycle is depicted in Figure 6c, exhibiting a RMSE of 27.7 mN. The box plot displayed in Figure 6d illustrates the error observed in eight distinct random load cycles, with a median RMSE value of 29.6 mN. The nonlinear term in the calibration curve has a negligible coefficient compared to the linear terms. However, removal of nonlinear factor results in an additional error in the measurement of force throughout the validation process.

1) *Static characteristics:* The static characteristics of the sensor for normal and shear force application are tabulated below.

Shear loading:

The increase in lateral displacement of indenter corresponds to an equivalent increase in the area of bubble's contour, as shown in Fig.6a. Shear load moves the contour in bilateral directions during the upward movement of indenter along the z-axis. The lateral deformation of the contour is shown in Fig.7a. Shear force increases as the indenter moves from periphery to center, and decreases as it moves from center to periphery of the bubble. This behavior is attributed to the bubble's protrusion on the elastomer surface, which is facilitated by the internal pressure within the bubble. Also, the magnitude of the shear force is proportional to the indenting normal force. We have calibrated the Subblescope for two conditions of shear. The first being the indenter is just in contact with the surface controlled by the screw gauge motion

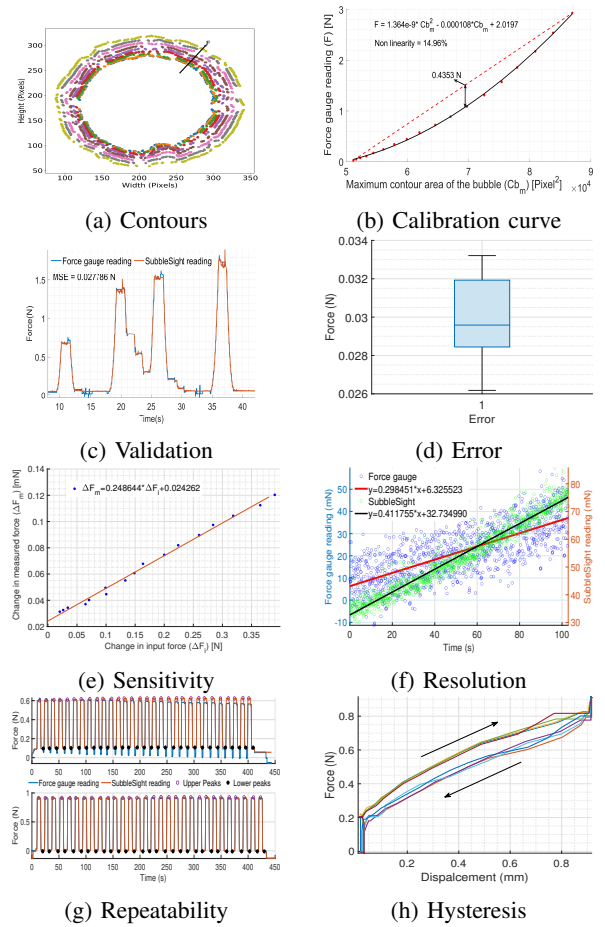


Fig. 6: The calibration and validation of Subblescope sensor for normal load. **a.** The change in the outer contour of the bubble with the application of normal force. **b.** The calibration curve with the corresponding functional form and the nonlinearity of the Subblescope for the maximum area of the bubble-contour (Cb_m) in Pixel^2 versus the force gauge reading ($F[N]$). **c.** The validation of the sensor, subjected to random normal forces for a single trial. **d.** The box plot shows the sensor's mean square error (MSE) for eight random load trials. **e.** The sensitivity of the sensor, varies over the change in input force. **f.** The resolution of the sensor. **g.** The repeatability of the sensor for thirty cycles in terms of coefficient of variance (COV). The upper, and lower figures show the repeatability of the sensor between 0.1 N to 0.6 N, and 0.1 N to 0.9 N respectively. **h.** The hysteresis of the sensor.

TABLE I: The calibration parameters for F_N and F_S . The shearing is induced by a normal compression at 0 N and 0.05 N by the indenter.

Static characteristics	F_N	F_S @0 N	F_S @0.05 N
Resolution	0.02 N	0.02 N	0.02 N
Range	0.02 N to 2.93 N	0.02 N to 0.075 N	0.02 N to 0.15 N
Sensitivity	248.6 μN	29.425 μN	31.31 μN
Offset	0.024 N	0.012 N	0.021 N
Repeatability	0 N - 2.57%, 0.1 N-2.76%, 0.6 N-1.09%, and 0.9 N-0.66%	-	-
Accuracy	0 N - 99.16%, 0.1 N - 96.07%, 0.6 N - 97.95%, and 0.9 N - 99.16%	-	-
Linearity	85.04 %	100.0%	100.0%
Hysteresis	0.1 N to 0.6 N - 26.23 μJ , 0 N to 0.9 N - 80.54 μJ	-	-
Dynamic characteristics	$t_r = 0.0475 \text{ s}$, $t_s = 0.7194 \text{ s}$ $\omega_n = 26.94 \text{ rad s}^{-1}$ $= 4.28 \text{ Hz}$, $\zeta = 0.2$		

of the X- θ rotary table. Similarly, the second condition is while the Subblescope is moved by 0.2 mm against the indenter which corresponds to a normal force of 0.05 N. The calibration curve for the second condition is shown in Fig.7b. When the depth of indentation reaches 0.2mm near the film, the film dissolves. Therefore, the range of F_S is contingent upon the thickness of the film around the bubble. The calibration curve follows a linear form as represented by equation (6).

$$\begin{aligned} F_c &= 29.425 \times 10^{-6} Cb_m - 1.574 \\ F_{nl} &= 31.31 \times 10^{-6} Cb_m - 1.674 \end{aligned} \quad (6)$$

where, F_c and F_{nl} are force gauge reading in N during indenter is in contact and indenter applying a normal load of 0.05 N to the Subblescope respectively, and Cb_m is the maximum contour of bubble as seen by camera in $Pixel^2$.

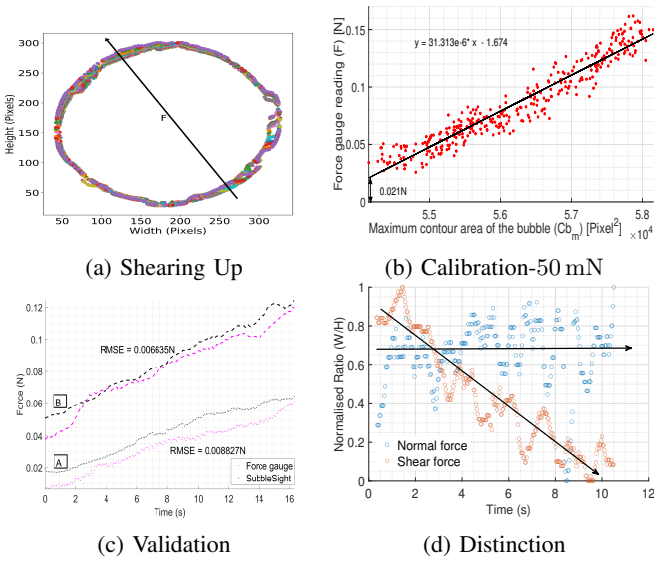


Fig. 7: The calibration and validation of Subblescope sensor for shear load and the dynamic characteristics. **a.** The change in the outer contour of the bubble with the application of shear force along Z+. **b.** The calibration curve of the sensor while the indenter applies a force of 0.05 N onto the surface of the Subblescope. **c.** The sensor is validated with the force gauge for an arbitrary ramped shear displacement of the indenter onto the sensor. **d.** The ratio of width (b) to height (a) of the bubble has a constant trend for normal and a declined trend for shear loading.

The calibration curve for shear load exhibits a linear response as evident from equation 6, in contrast to calibration curve of normal load. This is due to the range of force for shear load being lesser compared to normal load. The differentiation between shape of the bubble, due to normal and shear forces is determined by the ratio of width of minor to the major axis width ($r_{ba} = \frac{b}{a}$) of the bubble. The normal load does not shift r_{ba} drastically, but during shear, r_{ba} drops according to the magnitude of the shear force, as seen in Figure 7d. The validation of Subblescope for shear force within the specified range may be shown in Figure 7c. The RMSE between two measurements (force gauge and Subblescope) for just contact and with a contact force of 0.05 N is 8.8 mN, and 6.6 mN respectively.

2) Dynamics characteristics: The sensor's step response exhibits several dynamic properties, including response time (t_r), settling time (t_s), natural frequency (ω_n), damping ratio

(ζ), and drift. The step input is applied to the sensor by moving the indenter at a faster feed rate of 800 millimeters per minute. The Subblescope's reaction to the step input is depicted in Figure 8a, and it closely resembles the response of a second or a third order system. Consequently, we utilize Matlab to estimate the transfer function (TF_b) model by analyzing the input and output response, which consists of one zero and three poles. The transfer function is shown below.

$$TF_b = \frac{870s + 10590}{s^3 + 26.63s^2 + 896.4s + 11560} \quad (7)$$

where, TF_b is the transfer function of Subblescope. The time domain response from the TF_b for step input fits reasonably well with 90.31% to the experimental data.

The t_r , t_s , ω_n , and ζ are shown in Table-I, obtained from the transfer function in equation 7. The drift of Subblescope after a ramp and hold at different feed rates of the indenter is shown in Fig.8b. The drift is 1 mN to 5 mN, considering all the feed rates of 20, 100, 400, 800, and 1200 $mm\ min^{-1}$.

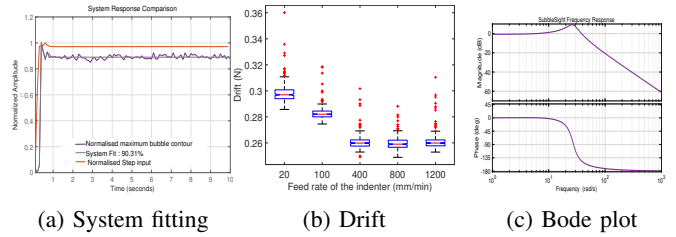


Fig. 8: **a.** The sensor's step response is depicted by a purple line, while the transfer function model is represented by a gray line. The orange line represents the input to the sensor at a feed rate of 800 $mm\ min^{-1}$. **b.** The drift of the sensor during step input at various feed rates of the indenter. **c.** The bode plot of the transfer function model.

VII. DISCUSSION

This work mimics the biological tissues, whose mechanics combine both solid and fluid structures to function effectively. It describes the unique VBHS, primarily through bubble dynamics inside a soft transparent elastomer. The viscous loss is negligible as the bubble is made up of air, whose viscosity (μ) is 18.6 $\mu Pa\ s$ [50].

The introduction of a bubble results in an increase in sensitivity to 248.6 μN , a resolution of 0.02 N, acceptable repeatability, and a lower hysteresis. The presence of bubble leads to a composite structure, nearly linear elastic in the lower range of force as shown during shear calibration. However, with a higher range of force, nonlinear factor becomes evident. The range of the sensor increases with the depth of the bubble from the point of application of force [51]. The range of sensor also depends on modulus of the elastomer. The use of elastomers with higher moduli, such as polydimethylsiloxane (PDMS) and polyrotaxane, improves range [52]. Additionally, the sensor's range is limited by the vanishing of the thin film. An increase in applied force causes a reduction in film-thickness of the bubble, causing destructive interference of reflected light waves from the inner and outer films [53]. The film desolution can be overcome by using highly-purified water ($\mu = 0.001 Pa\ s$), methanol ($\mu = 0.00056 Pa\ s$), and acetone ($\mu = 0.00031 Pa\ s$) [54] instead of air. However, it may acquaint viscoelasticity in the elastomer.

The dynamic characteristic shows the natural frequency of the single bubble composite elastomer as 4.28 Hz. It needs further study to deduce the natural frequency by varying the V_{inj} that decides the internal pressure inside the bubble. The controlled natural frequency enables the sensor to resonate with the physical stimuli to capture the signal with a better signal-to-noise ratio (SNR).

A. Challenges

There are several challenges in using bubbles as a force sensing element.

Bubble stability: The incorporation of a bubble into an elastomer is crucial. The bubble will be released if the value of μ_e is less than critical viscosity of elastomer, denoted as μ_e^c . If the viscosity of fluid (μ_e) is greater than critical viscosity (μ_e^c), the process of inserting a bubble might result in fractures at the boundaries. Therefore, the refractions occurring at the contact between bubble and elastomer cause the edges to appear blurred.

Film stability: The precise implantation of a bubble results in the formation of a stable bubble within an elastomer. Nevertheless, the thickness of the boundary film decreases when the load exceeds 3 N, as a result of destructive interference, which is a constraint of the current sensor.

B. Applications

Having a description of the sensor characteristics and challenges of Subblescope, it has numerous industrial and biomedical applications involving contact. The industrial applications can include estimating grasping force in robots to train them to handle objects without slip, texture detection (roughness, smoothness, hardness, etc), and measurement of wind velocity. Examples of biomedical applications can be rehabilitation for fine grasping, estimation of palpation force during ultrasound against soft tissues, pulse visualization from arteries, and haptics for force-based actuation in a virtual environment. Some of the applications are provided in the following section.

1) *Sphar-dynogram*: The radial artery pulsation is an active interface that provides a force feedback depending on the applied force onto it. The pulsation is captured by photoplethysmogram referring to a change in volume of blood [55]. Similarly, ‘*Sphar-dynogram*’ refers to the change in force of pulsatile artery measured by a bubble as shown in Fig. 9b. The word ‘*Sphar*’ originates from Sanskrit language, and it refers to a flaw caused by a bubble. The radial artery has been selected for recording force of the pulse due to its significance in the pulse diagnosis [56], [57] in Fig. 9a. The participants selected for testing the application have been approved by the Institutional Ethical Committee (IEC) of IIT Madras, with the reference number (IEC/2023 – 03/MM/02/03).

2) *Sphar-Whisker*: The Subblescope can be used for whisking [58] the surface to measure the roughness of it as shown in Figure 9c. The whisker is made up of carbon fiber [58] (diameter (d) = 0.8 mm, height (L) = 8 mm). The effective length of the whisker is 5 mm fitted in the conical PLA socket placed inside hard silicon rubber (Shore 50A) insert. The whisker assembly is placed on top of Subblescope for *Sphar-Whisking*. The set-up is moved at a feed rate of 50 mm s⁻¹ on

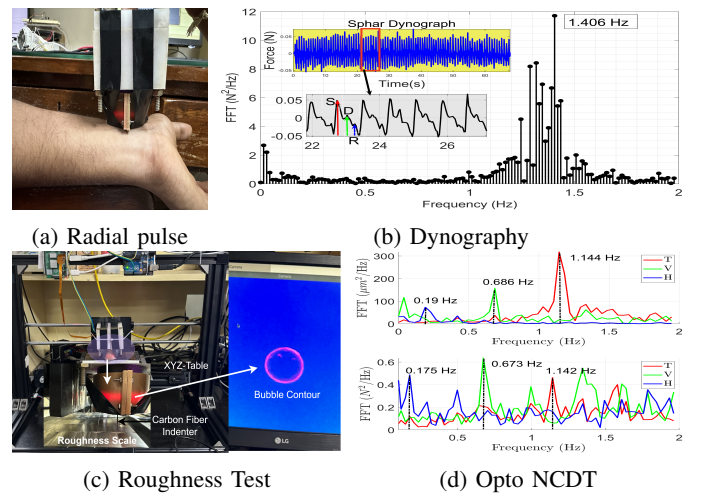


Fig. 9: a. Pulse force recording from the radial artery of a typical participant by attaching a cylindrical indenter onto the surface of Subblescope. b. *Sphar* dynography showing the distinct features (S-Systole, D- Diastole, R- Reflection waves) of pulse and heart rate of 84.36 bpm by Fourier transform of pulse force. c. *Sphar* whisking for the roughness of 50 μ m surface created from machining by turning (T), vertical milling (V), and horizontal milling (H). d. Spectrum of the roughness measured from laser meter and Subblescope.

50 μ m rough surface while recording the deformation in bubble contour caused by whisker movement. The surface for the exploration is the standard roughness scale is by RUBERT & Co. LTD., England [59]. The spectral analysis shows the similarity between the laser sensor and *Sphar-Whisker* sensor for turning (T), vertical milling (V), and horizontal milling (H) machined surfaces. The resemblance is in the frequency of the peak value in the Fourier spectrum. The values are 1.14 Hz, 0.68 Hz, and 0.19 Hz for T, V, and H machined surfaces from the laser sensor in Fig.9d. This corresponds to 1.14 Hz, 0.67 Hz, and 0.17 Hz obtained from *Sphar-Whisker* sensor in Fig.9d.

VIII. CONCLUSION

The flexible sensors have the ability to sense various haptic cues. Most of the flexibility is achieved by improving the hyperelasticity of the elastomer bonded with a sensor element to sense force, moment, temperature, proximity, morphology of surface in contact, etc. In this paper, the enhancement of hyperelasticity is achieved through a stable bubble in the elastomer, whose principles, algorithms, design, fabrication process, calibration, and application as a Subblescope sensor have been elucidated. The Subblescope has higher sensitivity and resolution compared to existing VBHSs for sensing fine touch. Moreover, the bidirectional sensing by Subblescope as a VBHS is a novel exploration to visualize arterial pulse. The use of Subblescope for measuring surface roughness has shown potential application in robotics. Investigating the film-stability and incorporation of numerous bubbles into the elastomer to improve spatial resolution will be a subject of future research.

REFERENCES

- [1] J. Byrne, V. Castellucci, and E. R. Kandel, “Receptive fields and response properties of mechanoreceptor neurons innervating siphon skin and mantle shelf in aplysia.” *Journal of Neurophysiology*, vol. 37, no. 5, pp. 1041–1064, 1974.

- [2] J. C. Yang, J. Mun, S. Y. Kwon, S. Park, Z. Bao, and S. Park, "Electronic skin: recent progress and future prospects for skin-attachable devices for health monitoring, robotics, and prosthetics," *Advanced Materials*, vol. 31, no. 48, p. 1904765, 2019.
- [3] M. Chen, W. Luo, Z. Xu, X. Zhang, B. Xie, G. Wang, and M. Han, "An ultrahigh resolution pressure sensor based on percolative metal nanoparticle arrays," *Nature communications*, vol. 10, no. 1, p. 4024, 2019.
- [4] J. A. Fishel and G. E. Loeb, "Sensing tactile microvibrations with the biotac—comparison with human sensitivity," in *2012 4th IEEE RAS & EMBS international conference on biomedical robotics and biomechatronics (BioRob)*. IEEE, 2012, pp. 1122–1127.
- [5] P. Payeur, C. Pasca, A.-M. Cretu, and E. M. Petriu, "Intelligent haptic sensor system for robotic manipulation," *IEEE Transactions on Instrumentation and Measurement*, vol. 54, no. 4, pp. 1583–1592, 2005.
- [6] H. Sun and G. Martius, "Machine learning for haptics: Inferring multi-contact stimulation from sparse sensor configuration," *Frontiers in neurobotics*, vol. 13, p. 51, 2019.
- [7] C.-B. Huang, Y. Yao, V. Montes-García, M.-A. Stoeckel, M. Von Holst, A. Ciesielski, and P. Samorì, "Highly sensitive strain sensors based on molecules–gold nanoparticles networks for high-resolution human pulse analysis," *Small*, vol. 17, no. 8, p. 2007593, 2021.
- [8] C. M. Boutry, M. Negre, M. Jorda, O. Vardoulis, A. Chortos, O. Khatib, and Z. Bao, "A hierarchically patterned, bioinspired e-skin able to detect the direction of applied pressure for robotics," *Science Robotics*, vol. 3, no. 24, p. eaau6914, 2018.
- [9] P. Mittendorf and G. Cheng, "Humanoid multimodal tactile-sensing modules," *IEEE Transactions on robotics*, vol. 27, no. 3, pp. 401–410, 2011.
- [10] J. R. Guadarrama-Olvera, F. Bergner, E. Dean, and G. Cheng, "Enhancing biped locomotion on unknown terrain using tactile feedback," in *2018 IEEE-RAS 18th International Conference on Humanoid Robots (Humanoids)*. IEEE, 2018, pp. 1–9.
- [11] M.-F. Lin, C. Cheng, C.-C. Yang, W.-T. Hsiao, and C.-R. Yang, "A wearable and highly sensitive capacitive pressure sensor integrated a dual-layer dielectric layer of pdms microcylinder array and pvdf electrospun fiber," *Organic Electronics*, p. 106290, 2021.
- [12] K. Shimada and N. Saga, "Mechanical enhancement of sensitivity in natural rubber using electrolytic polymerization aided by a magnetic field and mcf for application in haptic sensors," *Sensors*, vol. 16, no. 9, p. 1521, 2016.
- [13] J. Park, M. Kim, Y. Lee, H. S. Lee, and H. Ko, "Fingertip skin-inspired microstructured ferroelectric skins discriminate static/dynamic pressure and temperature stimuli," *Science advances*, vol. 1, no. 9, p. e1500661, 2015.
- [14] Y.-C. Lai, Y.-C. Hsiao, H.-M. Wu, and Z. L. Wang, "Waterproof fabric-based multifunctional triboelectric nanogenerator for universally harvesting energy from raindrops, wind, and human motions and as self-powered sensors," *Advanced Science*, vol. 6, no. 5, p. 1801883, 2019.
- [15] P. Piacenza, K. Behrman, B. Schifferer, I. Kymissis, and M. Ciocarlie, "A sensorized multicurved robot finger with data-driven touch sensing via overlapping light signals," *IEEE/ASME Transactions on Mechatronics*, vol. 25, no. 5, pp. 2416–2427, 2020.
- [16] H. Bai, S. Li, J. Barreiros, Y. Tu, C. R. Pollock, and R. F. Shepherd, "Stretchable distributed fiber-optic sensors," *Science*, vol. 370, no. 6518, pp. 848–852, 2020.
- [17] W. Yuan, S. Dong, and E. H. Adelson, "Gelsight: High-resolution robot tactile sensors for estimating geometry and force," *Sensors*, vol. 17, no. 12, p. 2762, 2017.
- [18] D. Ma, E. Donlon, S. Dong, and A. Rodriguez, "Dense tactile force estimation using gelslim and inverse fem," in *2019 International Conference on Robotics and Automation (ICRA)*. IEEE, 2019, pp. 5418–5424.
- [19] C. Sferazza and R. D'Andrea, "Design, motivation and evaluation of a full-resolution optical tactile sensor," *Sensors*, vol. 19, no. 4, p. 928, 2019.
- [20] R. Asahina, J. Wang *et al.*, "Development of a vision-based soft tactile muscularis," in *2019 2nd IEEE International Conference on Soft Robotics (RoboSoft)*. IEEE, 2019, pp. 343–348.
- [21] B. Ward-Cherrier, N. Pestell, L. Cramphorn, B. Winstone, M. E. Giannaccini, J. Rossiter, and N. F. Lepora, "The tactip family: Soft optical tactile sensors with 3d-printed biomimetic morphologies," *Soft robotics*, vol. 5, no. 2, pp. 216–227, 2018.
- [22] B. Lee, J.-Y. Oh, H. Cho, C. W. Joo, H. Yoon, S. Jeong, E. Oh, J. Byun, H. Kim, S. Lee *et al.*, "Ultraflexible and transparent electroluminescent skin for real-time and super-resolution imaging of pressure distribution," *Nature Communications*, vol. 11, no. 1, p. 663, 2020.
- [23] H. Sun, K. J. Kuchenbecker, and G. Martius, "A soft thumb-sized vision-based sensor with accurate all-round force perception," *Nature Machine Intelligence*, vol. 4, no. 2, pp. 135–145, 2022.
- [24] I. Andrussow, H. Sun, K. J. Kuchenbecker, and G. Martius, "Minsight: A fingertip-sized vision-based tactile sensor for robotic manipulation," *Advanced Intelligent Systems*, p. 2300042, 2023.
- [25] S. Okamoto, H. Nagano, and Y. Yamada, "Psychophysical dimensions of tactile perception of textures," *IEEE Transactions on Haptics*, vol. 6, no. 1, pp. 81–93, 2012.
- [26] J. Chodera and M. Lord, "Pedobarographic foot—pressure measurements and their applications," in *Disability: Proceedings of a seminar on rehabilitation of the disabled in relation to clinical and biomechanical aspects, costs and effectiveness, held at the University of Strathclyde, Glasgow, in August, 1978*. Springer, 1979, pp. 173–181.
- [27] K. Tanie, K. Komoriya, M. Kaneko, S. Tachi, and A. Fujikawa, "A high resolution tactile sensor," in *Proc. of 4th Int. Conf. on Robot Vision and Sensory Controls*, vol. 251, 1984, p. 260.
- [28] T. G. Strickler III, "Design of an optical touch sensing system for a remote manipulator." Ph.D. dissertation, Massachusetts Institute of Technology, 1966.
- [29] J. L. Schneiter and T. B. Sheridan, "An optical tactile sensor for manipulators," *Robotics and computer-integrated manufacturing*, vol. 1, no. 1, pp. 65–71, 1984.
- [30] H. Maekawa, K. Tanie, and K. Komoriya, "A finger-shaped tactile sensor using an optical waveguide," in *Proceedings of IEEE Systems Man and Cybernetics Conference-SMC*, vol. 5. IEEE, 1993, pp. 403–408.
- [31] D. Hristu, N. Ferrier, and R. W. Brockett, "The performance of a deformable-membrane tactile sensor: basic results on geometrically-defined tasks," in *Proceedings 2000 ICRA. Millennium Conference. IEEE International Conference on Robotics and Automation. Symposia Proceedings (Cat. No. 00CH37065)*, vol. 1. IEEE, 2000, pp. 508–513.
- [32] M. Ohka, Y. Mitsuya, K. Hattori, and I. Higashioka, "Data conversion capability of optical tactile sensor featuring an array of pyramidal projections," in *1996 IEEE/SICE/RSJ International Conference on Multisensor Fusion and Integration for Intelligent Systems (Cat. No. 96TH8242)*. IEEE, 1996, pp. 573–580.
- [33] K. Vlack, K. Kamiyama, T. Mizota, H. Kajimoto, N. Kawakami, and S. Tachi, "Gelforce: A traction field tactile sensor for rich human-computer interaction," in *IEEE Conference on Robotics and Automation, 2004. TExCRA Technical Exhibition Based*. IEEE, 2004, pp. 11–12.
- [34] K. Sato, K. Kamiyama, H. Nii, N. Kawakami, and S. Tachi, "Measurement of force vector field of robotic finger using vision-based haptic sensor," in *2008 IEEE/RSJ International Conference on Intelligent Robots and Systems*. IEEE, 2008, pp. 488–493.
- [35] K. Sato, H. Shinoda, and S. Tachi, "Vision-based cutaneous sensor to measure both tactile and thermal information for teleexistence," in *2011 IEEE International Symposium on VR Innovation*. IEEE, 2011, pp. 119–122.
- [36] J. Zhu, T. Li, S. Cai, and Z. Suo, "Snap-through expansion of a gas bubble in an elastomer," *The Journal of Adhesion*, vol. 87, no. 5, pp. 466–481, 2011.
- [37] J. A. Zimmerlin, N. Sanabria-DeLong, G. N. Tew, and A. J. Crosby, "Cavitation rheology for soft materials," *Soft Matter*, vol. 3, no. 6, pp. 763–767, 2007.
- [38] S. Kundu and A. J. Crosby, "Cavitation and fracture behavior of polyacrylamide hydrogels," *Soft Matter*, vol. 5, no. 20, pp. 3963–3968, 2009.
- [39] P. Garstecki, M. J. Fuerstman, M. A. Fischbach, S. K. Sia, and G. M. Whitesides, "Mixing with bubbles: a practical technology for use with portable microfluidic devices," *Lab on a Chip*, vol. 6, no. 2, pp. 207–212, 2006.
- [40] J. R. Lindner, "Microbubbles in medical imaging: current applications and future directions," *Nature reviews Drug discovery*, vol. 3, no. 6, pp. 527–533, 2004.
- [41] F. Ilievski, A. D. Mazzeo, R. F. Shepherd, X. Chen, and G. M. Whitesides, "Soft robotics for chemists," *Angewandte Chemie International Edition*, 2011.
- [42] R. F. Shepherd, F. Ilievski, W. Choi, S. A. Morin, A. A. Stokes, A. D. Mazzeo, X. Chen, M. Wang, and G. M. Whitesides, "Multigait soft robot," *Proceedings of the national academy of sciences*, vol. 108, no. 51, pp. 20400–20403, 2011.
- [43] A. D. Marchese, C. D. Onal, and D. Rus, "Autonomous soft robotic fish capable of escape maneuvers using fluidic elastomer actuators," *Soft robotics*, vol. 1, no. 1, pp. 75–87, 2014.
- [44] B. Winstone, G. Griffiths, C. Melhuish, T. Pipe, and J. Rossiter, "Tactip—tactile fingertip device, challenges in reduction of size to ready

- for robot hand integration,” in *2012 IEEE International Conference on Robotics and Biomimetics (ROBIO)*. IEEE, 2012, pp. 160–166.
- [45] A. Nolin, K. Pierson, R. Hlibok, C.-Y. Lo, L. V. Kayser, and C. Dhong, “Controlling fine touch sensations with polymer tacticity and crystallinity,” *Soft matter*, vol. 18, no. 20, pp. 3928–3940, 2022.
- [46] T. Haas, C. Schubert, M. Eickhoff, and H. Pfeifer, “A review of bubble dynamics in liquid metals,” *Metals*, vol. 11, no. 4, p. 664, 2021.
- [47] R. W. Ogden, G. Saccomandi, and I. Sgura, “Fitting hyperelastic models to experimental data,” *Computational Mechanics*, vol. 34, pp. 484–502, 2004.
- [48] O. Lopez-Pamies, P. P. Castañeda, and M. I. Idiart, “Effects of internal pore pressure on closed-cell elastomeric foams,” *International Journal of Solids and Structures*, vol. 49, no. 19–20, pp. 2793–2798, 2012.
- [49] S. Ando, “Consistent gradient operators,” *IEEE Transactions on Pattern Analysis and Machine Intelligence*, vol. 22, no. 3, pp. 252–265, 2000.
- [50] C. Beal, “The viscosity of air, water, natural gas, crude oil and its associated gases at oil field temperatures and pressures,” *Transactions of the AIME*, vol. 165, no. 01, pp. 94–115, 1946.
- [51] D. Subudhi and M. Manivannan, “Novel single bubble haptic sensor: Subblesight,” in *2023 IEEE SENSORS*. IEEE, 2023, pp. 1–4.
- [52] H. Gotoh, C. Liu, A. B. Imran, M. Hara, T. Seki, K. Mayumi, K. Ito, and Y. Takeoka, “Optically transparent, high-toughness elastomer using a polyrotaxane cross-linker as a molecular pulley,” *Science advances*, vol. 4, no. 10, p. eaat7629, 2018.
- [53] A. Glassner, “Soap bubbles: part 2,” *IEEE Computer Graphics and Applications*, vol. 20, no. 06, pp. 99–109, 2000.
- [54] V. V. Yaminsky, S. Ohnishi, E. A. Vogler, and R. G. Horn, “Stability of aqueous films between bubbles. part 1. the effect of speed on bubble coalescence in purified water and simple electrolyte solutions,” *Langmuir*, vol. 26, no. 11, pp. 8061–8074, 2010.
- [55] Y.-H. Kao, P. C.-P. Chao, and C.-L. Wey, “Design and validation of a new ppg module to acquire high-quality physiological signals for high-accuracy biomedical sensing,” *IEEE Journal of Selected Topics in Quantum Electronics*, vol. 25, no. 1, pp. 1–10, 2018.
- [56] V. Lad, *Secrets of the pulse: The ancient art of Ayurvedic pulse diagnosis*. Motilal Banarsidass Publishe, 2005.
- [57] H. Kim, J. Y. Kim, Y.-J. Park, and Y.-B. Park, “Development of pulse diagnostic devices in korea,” *Integrative medicine research*, vol. 2, no. 1, pp. 7–17, 2013.
- [58] H. Wegiriya, N. Herzig, S.-A. Abad, S. H. Sadati, and T. Nanayakkara, “A stiffness controllable multimodal whisker sensor follicle for texture comparison,” *IEEE Sensors Journal*, vol. 20, no. 5, pp. 2320–2328, 2019.
- [59] P. K. Routray, A. S. Kanade, K. Tiwari, P. Pounds, and M. Muniyandi, “Towards multidimensional textural perception and classification through whisker,” in *2022 IEEE International Symposium on Robotic and Sensors Environments (ROSE)*. IEEE, 2022, pp. 1–7.